

Discharge Promotes Melt and Formation of Submarine Ice-Shelf Channels at the Beardmore Glacier Grounding Zone

**Key Points:**

- Basal-melt rates within narrow basal channels on Beardmore Glacier are linked to subglacial meltwater discharge upstream
- Differences between the ice-base gradient direction and velocity direction cause the channels to migrate in Eulerian surface elevation data
- Melt within these channels is 27× larger than the average melt rate of the Ross Ice Shelf

Andrew O. Hoffman¹ , Howard Conway², Joséphine Anselin^{3,4} , Keith W. Nicholls³ , Jonathan Kingslake^{1,5} , Paul Winberry⁶ , Michelle Koutnik² , Knut Christianson² , and Pierre Dutrieux³ 

¹Lamont-Doherty Earth Observatory, Columbia University, Palisades, NY, USA, ²Department of Earth and Space Sciences, University of Washington, Seattle, WA, USA, ³British Antarctic Survey, Cambridge, UK, ⁴Department of Applied Mathematics and Theoretical Physics, University of Cambridge, Cambridge, UK, ⁵Department of Earth and Environmental Sciences, Columbia University, New York, NY, USA, ⁶Department of Geological Sciences, Central Washington University, Ellensburg, WA, USA

Supporting Information:

Supporting Information may be found in the online version of this article.

Correspondence to:

A. O. Hoffman,
aoh2111@columbia.edu

Citation:

Hoffman, A. O., Conway, H., Anselin, J., Nicholls, K. W., Kingslake, J., Winberry, P., et al. (2025). Discharge promotes melt and formation of submarine ice-shelf channels at the Beardmore Glacier grounding zone. *Journal of Geophysical Research: Earth Surface*, 130, e2024JF007921. <https://doi.org/10.1029/2024JF007921>

Received 8 JUL 2024
Accepted 22 JAN 2025

Abstract Using radar data from the Beardmore Glacier grounding zone, we image a narrow subglacial channel (300–500 m wide) that reaches a height of 200 m above the ambient ice-shelf draft. Using repeat ICESat-2 observations and Worldview digital elevation models, we show that this channel we observe with radar is part of a system of channels. These channels form near the grounding zone where the axis of the channels runs up-gradient in smoothed ice base elevation (perpendicular to smoothed ice base elevation contours). Downstream, these features are advected with the flow and expressed as Eulerian surface elevation change in differenced co-registered digital elevation models. Continuity calculations indicate that melt rates within the channel are at least 20 m yr⁻¹. Idealized one-dimensional plume modeling indicates these melt rates require substantial meltwater discharge and are geographically continuous extensions of subglacial conduits we image upstream of the grounding zone. These basal-melt rates are 27× higher than the ambient basal-melt rates in the Ross. Asymmetric melt across the width of the channel suggests there is cross-channel ocean boundary current that may affect the efficiency of energy exchange across the ice-shelf ocean boundary layer within the channel. This is consistent with recent model experiments that suggest ice shelf basal channel shape determines channelized ice-ocean interactions.

Plain Language Summary Ice shelves are floating extensions of glaciers that buffer the flow of ice grounded on land to the ocean. Because ice shelves influence the rate of ice discharge to the ocean, ice-shelf melt can drive grounded ice volume change upstream. Localized melt can form and erode channels into the bottom of ice shelves, thinning the ice shelf by hundreds of meters. The impact of these localized channels on melt rates and the structural integrity of ice shelves is still unclear. Here, we report on geophysical studies of a system of large (~200 m high) subglacial melt channels discovered where Beardmore Glacier goes afloat and flows from East Antarctica into West Antarctica's Ross Ice Shelf. In the Ross Ice Shelf ocean cavity, ocean water temperatures are near the freezing point, limiting the capacity of the ocean to melt the base of the ice shelf. Despite these relatively low temperatures, our data reveal a melt channel with a geometry that implies the ocean is melting the bottom of the ice shelf at a rate exceeding 20 m per year. Our data indicate that this channel forms due to the drainage of fresh, buoyant subglacial meltwater from under the grounded ice, which entrains warmer ocean water into a buoyant plume and promotes more vigorous melt.

1. Introduction

Ice shelves, the floating extension of marine outlet glaciers, mediate mass exchange between the ocean and the ice sheet through basal melt, and accretion (Paolo et al., 2015; Reese et al., 2018; Rignot et al., 2019). Ice shelves melt at their base due to heat from warm ocean water that is entrained in out-flowing buoyant overturning circulation generated from basal melt or subglacial discharge. Basal melting beneath Antarctic ice shelves is currently responsible for as much as half of total ice-shelf mass loss (Rignot et al., 2019), and is projected to increase this century (Cai et al., 2023; Naughten et al., 2023). Increased basal melt responsible for ongoing changes in mass balance and projected future changes have been connected to increases in transport of warm, saline, modified circumpolar deep water across the continental shelf break. However, oceanic processes local to ice-shelf cavities can also affect heat transport and the efficiency of heat transfer at the ice-ocean interface (i.e., Cheng et al., 2024).

© 2025. The Author(s).

This is an open access article under the terms of the [Creative Commons Attribution License](https://creativecommons.org/licenses/by/4.0/), which permits use, distribution and reproduction in any medium, provided the original work is properly cited.

These processes include strong feedbacks between properties of the ice-shelf ocean boundary layer and the geometry of the ice-shelf cavity that remain less well studied because of the difficulties measuring properties of the ice-ocean boundary layer and mapping the ice-ocean interface (i.e., Cheng et al., 2024).

One of the strongest examples of this feedback is ice-shelf basal-melt channels that focus outflow and locally enhance ice-shelf melt rates. Basal channels are pervasive across Antarctica and have been detected using surface slopes expressed in satellite imagery (e.g., Rignot & Steffen, 2008), digital surface elevation models (e.g., Alley et al., 2019; Chartrand & Howat, 2020; Howat et al., 2019; D. E. Shean et al., 2019), autonomous underwater vehicle observations (e.g., Dutrieux et al., 2014; Stanton et al., 2013), and ice-penetrating radar technology (e.g., Le Brocq et al., 2010; Rignot & Steffen, 2008; Stanton et al., 2013). Basal-melt channels have been linked to a variety of source mechanisms sustained by the entrainment of heat into confined buoyant freshwater plumes (Sergienko, 2013). Some channels form where feedbacks allow positive melt-rate anomalies to grow with enhanced outflow (ocean driven; Sergienko, 2013). Other channels initiate where lateral variations in bed topography at the grounding zone form local variations in ice-shelf draft inherited as ice ungrounds over rough terrain (topography inherited; Drews et al., 2017). Channels can also form near the grounding zone from buoyant plumes that arise from subglacial discharge (discharge-driven; Le Brocq et al., 2013).

Catalogs of basal channels and roughness at the ice-shelf base have been used to diagnose these source mechanisms in the hydrographic and spatial context of different ice-shelf cavities (Alley et al., 2016, 2024; Watkins et al., 2021). These studies have hypothesized that melt channels and terrace features are strongly connected to the thermal driving of the ice-shelf cavity. Within “warm ice-shelf cavities” (e.g., Pine Island Ice Shelf; Dutrieux et al., 2014) where modified Circumpolar Deep Water circulating onto the continental shelf is able to reach the grounding zone, basal-melt rates are high ($\sim 5\text{--}200$ m/yr), and basal channels are common compared to “cold ice-shelf cavities” (e.g., Ross Ice Shelf) where melt is driven by the advection of High-Salinity Shelf water (HSSW) to the grounding zone. In cold shelf cavities, HSSW retains heat available for melting due to the pressure dependence of the melting point (Nicholls et al., 2009), basal-melt rates are typically low (<5 m/yr), and channelized melt is often linked to subglacial discharge (Le Brocq et al., 2013; Marsh et al., 2016; Whiteford et al., 2022).

Understanding the mechanisms that control the initiation and evolution of basal channels is important, as basal channels may impact the structural integrity of ice shelves and grounded ice discharge upstream (Rignot & Steffen, 2008). Modeling and observations indicate that ice-shelf basal melting reduces buttressing to grounded ice and that concentrated melting in basal channels can influence the flow and stability of ice shelves. Depth-integrated plume models have also been coupled to ice-flow models to investigate the mutual dependence of focused meltwater outflow and basal channel evolution and suggest that channels decrease the total shelf average melt rate compared to shelves where melt is not channelized (Gladish et al., 2012; Millgate et al., 2013).

Recent high-resolution simulations have also demonstrated the importance of vertical shear and thermohaline structure of sub-ice boundary currents that control turbulent heat exchange and melt at the ice-ocean interface (Burchard et al., 2022; Rosevear et al., 2022; Vreugdenhil & Taylor, 2019). In idealized high-resolution vertically resolved models of meltwater outflow, the increase in height and, thus, steepening of the channel flank were shown to determine melt magnitude by controlling both the friction velocity and near-ice temperature at the peak of the channel (Cheng et al., 2024). These experiments have shown that channelized basal melting of ice may be controlled by the cross-sectional channel geometry, particularly the channel height and the slope of the channel side walls. This modeled dependence of melt rate on channel geometry has not previously been linked to observations.

Here, we report on a system of nine large (100–200 m tall) and narrow (300–500 m wide) ice-shelf basal channels that form at the grounding zone of Beardmore Glacier (Figure 1). Beardmore Glacier conveys ice from East Antarctica through the Transantarctic Mountains to the Ross Ice Shelf, which sits above a “cold ice-shelf cavity” in the Ross Sea. The channels we survey at the terminus of the Beardmore Glacier outnumber the total number of basal channels identified previously for the entire Ross Ice Shelf. The channels and their expression in surface elevation data require melt rates in excess of 20 m yr^{-1} and are consistent with melt rates that have been observed near the grounding zone of “warm ice-shelf cavities” such as Pine Island Glacier (Figure 1). We use this system of channels to investigate the thermal driving of the Beardmore Glacier grounding zone.

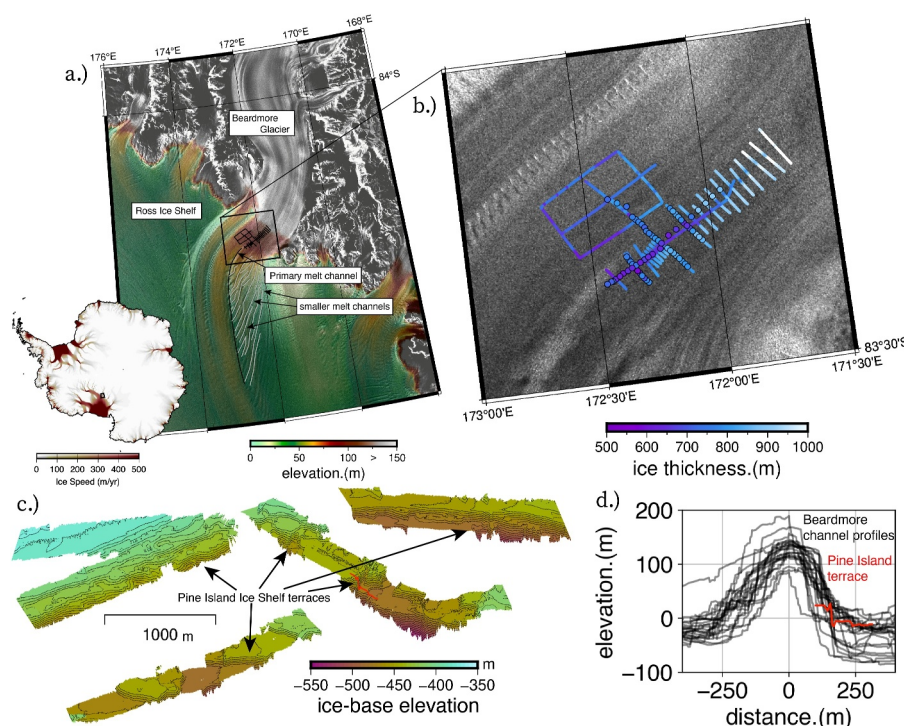


Figure 1. Survey overview with inset image of Antarctic surface speeds from Mouginot et al. (2019) with map of the Beardmore Glacier grounding zone and the Ross Ice Shelf overlaying RADARSAT-1 mosaic. Colormap shows Reference Elevation Model of Antarctica (Howat et al., 2019). Black lines indicate radar profiles crossing a system of basal channels visible in panel (a) surface elevation model with (b) thicknesses derived from profiling radar and pRES data. (c) Terrace features observed with an autonomous underwater vehicle from Pine Island Glacier (Dutrieux et al., 2014) shown with (d) anomalies of ice-base elevation profiles of the Beardmore channel shown with the ice base of terraces from Pine Island Glacier. Cross-sectional profiles of the primary Beardmore channel reveal asymmetry, with the western (right) channel wall sloping more steeply than the eastern channel wall (left).

2. Data and Methods

This study is the first to survey and document the system of subglacial channels across the Beardmore Glacier grounding zone. The data that we present were collected in 2012 as part of an airborne and ground-based campaign that collected ~600 km of impulse radar data that, combined with existing satellite-derived surface velocity and surface elevation fields, comprise one of the most complete surveys of an Antarctic grounding zone to date.

2.1. Ice-Penetrating Radar

A bespoke impulse ice-penetrating radar system was used to map the ice/ocean interface geometry and englacial layers. Ground-based radar profiles were collected using dipole antennas with a center frequency of 7 MHz. Airborne profiles were collected by towing the same system behind a Twin Otter aircraft (Conway et al., 2009), using antennas with a center frequency of 2 MHz. Following Christianson, Jacobel, et al. (2016), processing steps included bandpass filtering, time correction for antenna separation, geolocation from dual-frequency GNSS data, interpolation to a standard trace spacing of 5 m, and along-track time-wavenumber migration (Figure 2. See Text S1 in Supporting Information S1). Using ice thickness and geolocation information, we calculate the height above floatation (Figure S1 in Supporting Information S1). Basal and englacial reflectors were digitized using a semi-automated routine that identified the Ricker wavelet corresponding to the local maximum and two surrounding local minima of the reflector interface (Christianson, Jacobel, et al., 2016; Gades et al., 2000; Lilien et al., 2020). We calculate bed-returned power after correction for geometric spreading and englacial attenuation following Matsuoka et al. (2010) and Christianson, Jacobel, et al. (2016) (See Texts S2, S3 and Figures S2, S3 in Supporting

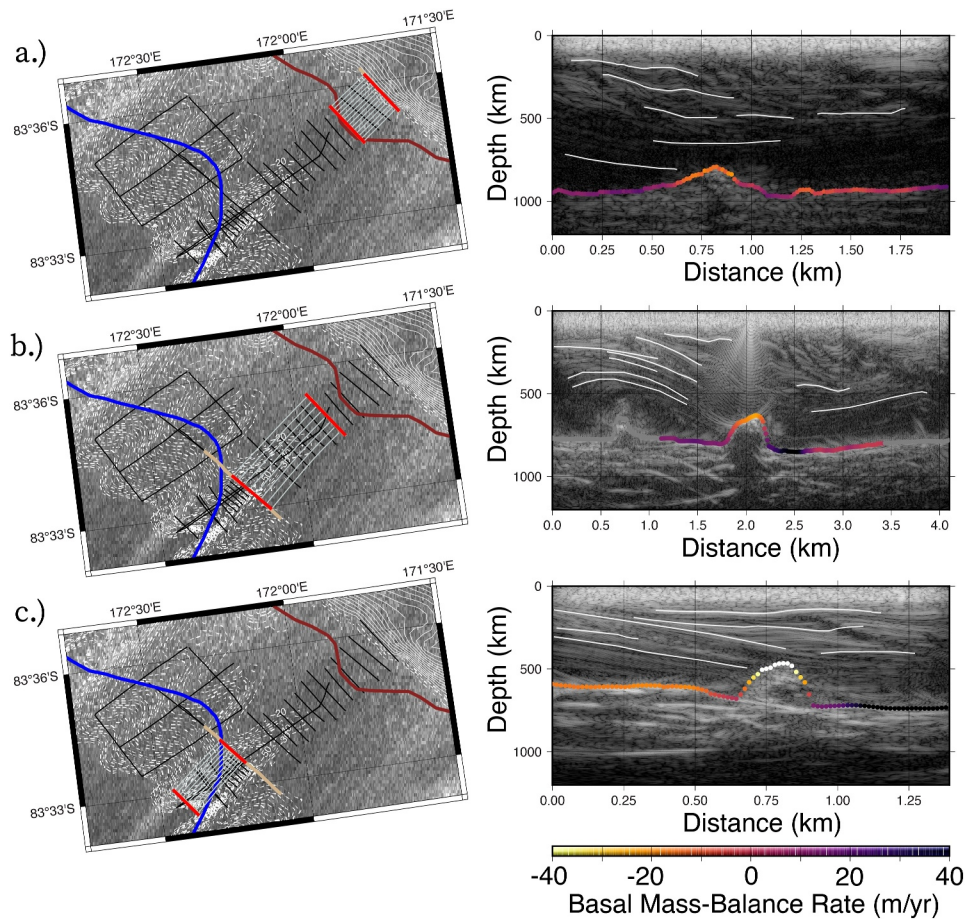


Figure 2. Overview of the channel with flowlines used to estimate volume flux along the channel for panels (a–c) different cross-sections of the melt channel. Digitized layers in radargrams are shown in white.

Information S1). We combine the ice-shelf geometry determined from ice-penetrating radar observations of ice thickness with observations of surface velocity to constrain the volumetric flux associated with melt across the width of the channel. This calculation assumes a linear vertical deformation profile with depth and that the system is in steady state.

2.2. Stereo Digital Elevation Models and ICESat-2 Laser Altimetry

Digital elevation models (DEMs) from Worldview stereo imagery of the Beardmore Glacier grounding zone were used to construct a time series of surface elevation changes near the ice-shelf channel we image with ice-penetrating radar. Following Nuth and Kääb (2011) and D. E. Shean et al. (2019), elevation observations from Worldview digital elevation models were co-registered with one another using a mask for bare ground and stagnant grounded ice reservoirs (surface flow speeds < 10 m/yr). From these referenced elevation models (Figure 3, Figure S4 in Supporting Information S1), we map the system of channels using the flow accumulation, a metric that describes the number of cells upstream flowing into each cell according to the static hydropotential defined by an elevation model (Bartos, 2020). We resample each co-registered elevation model at 50 m and use a 1.25 km radial Gaussian kernel to smooth each product and calculate the flow accumulation of each digital elevation model using the smoothed surface gradient. The flow accumulation was then used to delineate the thalweg of the surface (the line or curve of lowest elevation within a valley) that has an upstream catchment area of at least $5,000$ m². Using distributed surface velocities derived by Mouginot et al. (2019), we backtrace the location of each thalweg to 2014 (Figure 3c) based on the difference between the associated elevation model and a

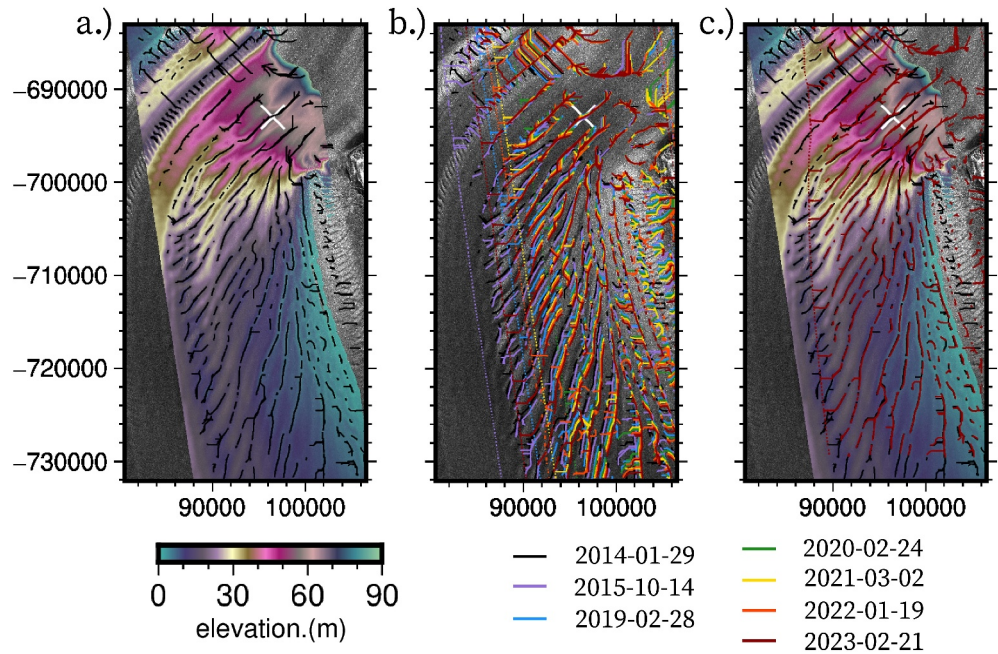


Figure 3. (a) Surface elevation over the Beardmore channel in the austral summer of 2014 with the network of channels identified using the flow accumulation of the surface elevation to map the thalweg. (b) Channel positions in time identified from the flow accumulation used to map the thalweg from 2014 to 2023. (c) Channel locations from 2023-02-21 backtraced to the position in 2014-01-29 using annual flow velocities from 2017 (Mouginot et al., 2019).

reference model (from 1 February 2014), which uses satellite data from the same year that much of the ground-based data were collected.

These precise spatially distributed high-resolution digital elevation models complement precise repeat elevation observations along profiles made with ICESat-2 (Figure S5 in Supporting Information S1). ICESat-2 is a polar-orbiting satellite equipped with the Advanced Topographic Laser Altimeter System (ATLAS), a state-of-the-art photon-counting laser altimeter. The instrument precisely repeats the same tracks every 91 days, making it particularly useful for measuring surface height change signals and ice-shelf response to localized melt (Chartrand & Howat, 2020; B. E. Smith et al., 2009). We used descending ICESat-2 orbits and the cloud computing SlideRule package to convert geolocated photons to ice-sheet elevation averaged along 10 m overlapping segments of 5 m spacing using all photon data exceeding the medium confidence threshold (D. Shean et al., 2023). The 10 m length of along-track averaged segments was chosen to resolve the confined nature of the channel and surface crevasses that appear to run along either side of the channel parallel to the ice-flow direction (Figure S5 in Supporting Information S1).

2.3. Basal Channel Mass Balance From Continuity

Across the channel, we estimate basal mass balance from ice thickness and surface velocity measurements following the mass conservation technique used by Jenkins (1991). Assuming a steady-state ice thickness and assuming that the horizontal divergence of the volume flux is balanced by the surface and basal mass balance rate, we can express basal mass balance from a simplified version of the continuity equation as:

$$\dot{m}_b = v \frac{\partial H}{\partial x} + (\dot{\epsilon}_x + \dot{\epsilon}_y) H - \dot{a} \quad (1)$$

where the x -axis is the flow direction, v is the along-flow ice speed, \dot{a} and \dot{m}_b are the surface and basal mass balance rates, respectively, H is the ice thickness, and $\dot{\epsilon}_x$ and $\dot{\epsilon}_y$ are the longitudinal and transverse strain rates (Jenkins, 1991). We simplify this calculation by implementing it along flowlines, which were selected to originate

Table 1
Model Parameters and Parameter Values

Parameter	Symbol	Value
Entrainment coefficient	E_0	$3.6e^{-2}$
Drag coefficient	C_d	$1.5e^{-3}$
Thermal Stanton number	$C_d^{1/2} \Gamma_T$	$4.7e^{-4}$
Haline Stanton number	$C_d^{1/2} \Gamma_S$	$1.4e^{-5}$
Freezing point salinity coefficient	λ_1	$-5.73e^{-2} \text{ } ^\circ\text{C}$
Freezing point offset	λ_2	$8.32e^{-2} \text{ } ^\circ\text{C}$
Freezing point depth coefficient	λ_3	$7.61e^{-4} \text{ } ^\circ\text{C m}^{-1}$
Thermal expansion coefficient	β_T	$3.87e^{-5}$
Haline contraction coefficient	β_S	$7.86e^{-4} \text{ } \text{psu}^{-1}$
Specific heat capacity of ocean water	c_w	$3.974e^3 \text{ J kg}^{-1} \text{ } ^\circ\text{C}^{-1}$
Specific heat capacity of ice	c_i	$2.009e^3 \text{ J kg}^{-1} \text{ } ^\circ\text{C}^{-1}$
Latent heat of fusion of ice	L	$3.35e^5 \text{ J kg}^{-1}$
Temperature of ice	T_i	-15°C
Salinity of ice	S_i	$0 \text{ } \text{psu}$
Gravitational acceleration	g	9.81 m s^{-2}
Reference seawater density	ρ_0	$1,030 \text{ kg m}^{-3}$
Slope of the ice draft	α	–
Ambient cavity temperature	T_a	–
Ambient cavity salinity	S_a	–
Boundary layer temperature	T_b	–
Boundary layer salinity	S_b	–

on upstream transverse-to-flow profiles, that flow through profiles downstream. Along flowlines, this calculation simplifies to:

$$\bar{m}_b = \bar{v} \frac{H_d - H_u}{\Delta x} + \left(\bar{\epsilon}_x + \bar{\epsilon}_y \right) \bar{H} - \bar{a} \quad (2)$$

where we consider spatially averaged values for parameters between the flowlines, H_d and H_u are the downstream and upstream ice thicknesses determined from the radar data, and Δx is the length of the flowline between the two transverse radar lines. Flowlines and velocities were determined from the ice velocity field produced by Mougino et al. (2019). Surface strain rates, assumed to be representative of depth-averaged strain rates, were calculated from the same velocity field (Figure S6 in Supporting Information S1; Mougino et al., 2019) following the logarithmic strain rate methodology of Alley et al. (2018) using a smoothing length scale of 1,000 m. Since our data are too sparse to create an ice-thickness grid, average ice thicknesses were interpolated along flowlines using the thickness field of BedMachine Antarctica (Morlighem et al., 2020).

2.4. Ocean Plume Model

To understand the oceanographic conditions that promote the basal-melt rates we calculate from continuity assumptions, we turn to idealized representations of a meltwater plume (Morton et al., 1956). We adapt radially averaged plume theory (Cowton et al., 2015) to evaluate the sensitivity of basal-melt rates near the Beardmore Glacier grounding zone to variability and uncertainty in the ambient cavity ocean temperatures and subglacial discharge flux (Figure 5a). The prognostic variables of this model are the plume radius b , velocity u , temperature T , and salinity S . The model conserves mass, momentum, heat and salinity according to four equations.

$$\frac{d}{dz}(b^2 u) = 2b\dot{e} + \frac{4}{\pi} b \dot{m} \quad (3a)$$

$$\frac{d}{dz}(b^2 u^2) = gb^2 \frac{\rho_a - \rho_p}{\rho_0} \sin(\alpha) - \frac{4C_d}{\pi} b u^2 \quad (3b)$$

$$\frac{d}{dz}(b^2 u T) = 2b\dot{e} u T_a + \frac{4}{\pi} \dot{m} b T_b - \frac{4\Gamma_T C_d^{1/2}}{\pi} b u (T - T_b) \quad (3c)$$

$$\frac{d}{dz}(b^2 u S) = 2E_0 b u S_a + \frac{4}{\pi} \dot{m} b S_b - \frac{4\Gamma_S C_d^{1/2}}{\pi} b u (S - S_b) \quad (3d)$$

Symbols and parameter values are defined in Table 1. The model differs slightly from Cowton et al. (2015) in that the geometric spreading of the plume is confined to the base of the shelf rather than a submerged vertical ice-cliff face. The entrainment rate is thus defined as a linear function of the plume velocity and sine of the interface slope

$$\dot{e} = E_0 u \sin \alpha. \quad (4)$$

The plume model couples the buoyant plume theory described above and the standard three-equation basal-melt parametrization (Holland & Jenkins, 1999; McPhee et al., 1987) to compute basal-melt rates along the ice-ocean interface.

$$\dot{m}(c_i(T_b - T_i) + L) = \Gamma T C_d^{1/2} u c_w (T - T_b) \quad (5a)$$

$$\dot{m}S_b = \Gamma_S C_d^{1/2} u c_w (T - T_b) \quad (5b)$$

$$T_b = \gamma_1 S_b + \gamma_2 + \gamma_3 z \quad (5c)$$

The subglacial discharge was modeled by imposing an initial freshwater discharge flux at the grounding line consistent with assumptions for the upstream flux and R othlisberger channel theory. The drag coefficient and the thermal and haline Stanton numbers were chosen based on values recommended by Stewart (2018) for the Ross Ice Shelf. We use an idealized ice-shelf draft similar to the observed draft of Beardmore Glacier, which has a grounding-line depth of 900 m, a steep region with a basal slope of 0.005 extending 10 km from the grounding line, and a nearly flat ice base with a slope of 0.001 extending a farther 590 km to the ice front. Along-flow basal slopes near the grounding line were calculated from the apex of the observed channel in ice-penetrating radar data and basal slopes downstream were calculated from freeboard observations of surface elevation. The initial discharge flux was varied between 1.0×10^{-6} and $0.1 \text{ m}^2/\text{s}$. The subglacial discharge flux was varied between values from regions of Antarctica where discharge can be ignored and summer discharge fluxes observed at Greenland outlet glaciers (Mernild et al., 2010), which are likely to exceed the discharge fluxes for Antarctic ice streams. Ambient ocean temperature was varied between -2.5 and -1.5°C . The temperature range was selected to include the conditions expected in the vicinity of Beardmore Glacier, estimated to be between -2.2 and -1.9°C based on measurements through the HWD-2 borehole in the Ross Ice Shelf (Stevens et al., 2020).

3. Results

3.1. Channel Expression in Radargrams

Basal channels are the most prominent feature of the radar survey. The primary channel we image with radar is profiled in several radar transects, including transects that cross the channel inland of the grounding zone. The channel grows from a height of ~ 30 m and width of ~ 190 m inland of the grounding zone (Figure 2) to a height of 200 m and a width of 500 m, 15 km downstream (Figure 1).

Ice base and surface elevation observations near the channel corrected for firm air content suggest that ice near the channel sits above flotation (Figure S1 in Supporting Information S1), and these differences in the height above flotation are larger than changes anywhere else downstream of the grounding zone. Gradients in height above flotation reveal where bridging stresses induce secondary flow that is also expressed in englacial stratigraphy (Figure 2). Englacial layers are disrupted and slope downwards, forming synclines over the center of the channel (Figure 2). These profiles also reveal that the channel geometry is asymmetric about the axis of the channel. Northwestern channel-wall slopes are steeper than southeastern wall slopes (Figure 2, Figure S2 in Supporting Information S1), and this asymmetry becomes more pronounced farther from the grounding zone as the channel incises deeper into the ice shelf (Figure 2). This asymmetry is also expressed in asymmetric surface slopes across the channel observed in ICESat-2 surface elevation profiles (Figure S5 in Supporting Information S1).

In addition to the morphology of the channel we see expressed geometrically in the radar imagery, we also see signals expressed in the reflection amplitude. Basal reflectivity is an indirect indicator of basal roughness, including roughness amplitude below the radar's vertical resolution, due to reflectivity decreases from diffuse scattering off rough interfaces (Christianson, Bushuk, et al., 2016; Hills et al., 2020; MacGregor et al., 2015). In this survey (see Text S3 in Supporting Information S1), basal reflectivity changes as the ice transitions from grounded to floating and near the basal channel. At the grounding zone, the basal reflectivity is relatively uniform and consistent with power returned from an ice/freshwater till interface (5–10 dB; Figures S2 and S3 in Supporting Information S1). Basal reflectivity increases as the ice goes afloat, brightening by ~ 10 dB in transects 5 km downstream of the most inland profile (Figure S3 in Supporting Information S1). Reflectivities farther seaward are generally bright and consistent with reflections from an ice-seawater interface, except in the vicinity of the channel. Near the channel, reflectivity is lower for all profiles, likely due to basal roughness associated with terraces and reflections from steep channel walls that do not return to the receiver.

At the grounding zone, the channel is already ~ 30 m tall and ~ 190 m wide (Figure 2, Figure S2 in Supporting Information S1). Fifteen kilometers from the grounding zone, the channel grows to a height of 200 m and a width of 500 m (Figure 1). The presence of a ~ 30 m high channel inland of the grounding zone suggests that subglacial meltwater outflow is focused and that turbulence-driven subglacial melt is active where the glacier is otherwise

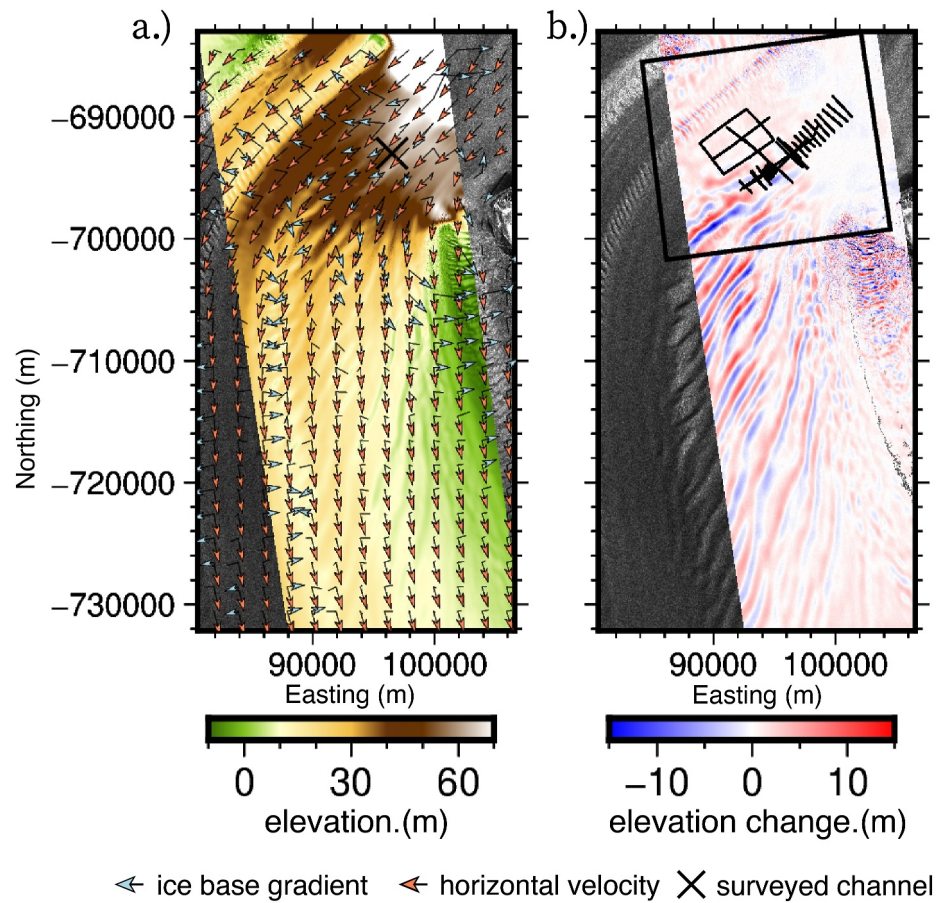


Figure 4. (a) The surface elevation of the Beardmore Glacier grounding zone is shown with the direction of the ice-base gradient (light blue arrow) and the ice velocity (orange arrow). Black X indicates channel location in radar data. (b) Surface elevation change from differences in coregistered elevation models. Radar profiles are shown in black. Black box indicates bounds from Figure 1b.

grounded. Though observed previously (Drews et al., 2017, 2020; Le Brocq et al., 2013; Marsh et al., 2016), this study presents new, unambiguous evidence of large channels under grounded ice seeding submarine ice-shelf melt channels. Assuming a semi-circular channel cross-section and a pressure gradient along the channel of 30 Pa/m, consistent with surface slopes, the single channel we survey at the grounding zone with radar is large enough to accommodate the entire modeled subglacial discharge ($\sim 8 \text{ m}^3/\text{s}$) from Beardmore Glacier (Willis et al., 2016). The scale of the channel is consistent with terraced landscapes observed elsewhere in Antarctica (Figure 1). Whilst such features have to date been observed in “warm ice-shelf cavities,” these are the first observations of terraced scale features within a “cold ice-shelf cavity” (Figure S7 in Supporting Information S1).

3.2. Surface Expression of Melt Channels

In addition to the primary channel we map in our radar survey, radar profiles also reveal two smaller basal channels mapped at the edges of the survey that are co-located with surface depressions visible in elevation models and SAR imagery downstream (Figure 3a). A map of depressions in surface elevation models from 2014 is shown in Figure 3 with the original surface elevation model used to calculate the thalweg and identify channels from the flow accumulation (Figure 3a). The time series of these channels from 2014 to 2023 is shown in Figure 3b. From Worldview stereo image pairs and repeat ICESat-2 elevation transects of the Beardmore Glacier grounding zone, we find that the primary channel is one of at least nine channel features expressed in surface elevation models (Figures 3 and 4, Figure S7 in Supporting Information S1). The system of channels migrates northwestward (coordinate reference system EPSG:4326) in Eulerian surface height change products generated

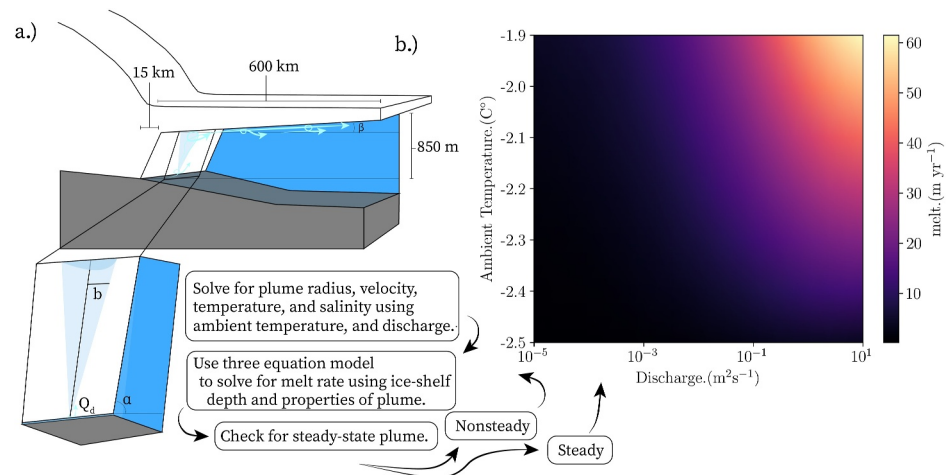


Figure 5. (a) Schematic of the plume model used to evaluate (b) the sensitivity of melt rate to discharge and ambient cavity temperature. The schematic shows the geometry of the simplified plume near the grounding zone of Beardmore Glacier with an ice shelf that slopes steeply up for 15 km before sloping more gently to the calving front for another 600 km.

for all years that we have observations (Figure 3 and Figures S6, S7 in Supporting Information S1). Correcting for ice advection, these channels mapped using the thalweg expressed in surface elevation models from 2015 to 2023 show no significant Lagrangian motion except for the area near the grounding zone, where we also observe the channel growing in ice-penetrating radar data. This suggests that the Beardmore channels advect with ice flow once they reach a critical distance from the grounding zone (~ 10 km) or critical ice-shelf draft (~ 600 m). Near the grounding zone in our radar survey, the Lagrangian channel position migrates eastward (Figure 3, Figure S7 in Supporting Information S1). In this region, the smoothed ice-base gradient is also oriented east of the flow direction (Figure 3). As the channels are advected, they create Eulerian elevation change anomalies as channel keels upstream advect into what were previously channel peaks downstream. This explains the apparent changes in ice elevation near the grounding zone and downstream and can be explained without invoking Coriolis forced migration (Alley et al., 2024).

3.3. Impact of Subglacial Discharge on Channel Melt Rates

Using surface strain rates (Figure S4 in Supporting Information S1) and cross-channel profiles of ice-shelf thickness with Equation 2 that describes mass continuity between profiles (Jenkins, 1991), we calculate a maximum basal-melt rate between 20–40 m/yr across the channel (Figure 2). These melt rates are high for cold ice-shelf cavities, approaching melt rates observed within warm cavity environments like the Thwaites and Pine Island Glacier (D. E. Shean et al., 2019). To understand the mechanisms that could promote these high melt rates, we turn to idealized simulations of a meltwater plume consistent with the geometry of the Beardmore Glacier grounding zone (Figure 5).

In all simulations, melt rates are highest near the grounding zone and decrease (sometimes promoting accretion) as the ice-shelf draft thins. Average melt rates as a function of ambient temperature and discharge flux over the first 10 km of the ice shelf are shown in Figure 5. These results hold across realistic ranges and measured values for transfer coefficients and other parameters that control the efficiency of the discharge-driven plume (see Supplement for details). We find that subglacial meltwater discharge fluxes must exceed $0.05 \text{ m}^2 \text{ s}^{-1}$ for melt rates to exceed 10 m/yr (the order of magnitude that we would infer from radar observations and surface velocities). This localized flux is similar to the width-averaged flux that is typically assumed for Greenland outlet glaciers. Confined to a point source, meltwater discharge fluxes cited for Beardmore Glacier (Willis et al., 2016) can promote melt rates exceeding 20 m/yr. This suggests that the channel we observe inland of the grounding zone and the large discharge flux required to open this channel inland of the grounding zone are important for entraining ocean heat, which then enhances melting near the Beardmore Glacier grounding zone.

4. Discussion

Ross Ice Shelf cavity circulation is dominated by HSSW formation that produces temperatures near the surface freezing point (MacAyeal, 1984). The density and depth of HSSW facilitate HSSW transport to grounding zones in the eastern Ross ice-shelf cavity well beyond the reach of surface waters and modified Circumpolar Deep Water (Jendersie et al., 2018). The thermal driving of HSSW is low and produces locally enhanced melt rates (3 m/yr Jendersie et al., 2018) that when averaged over the area of the shelf are consistent (~ 9 cm/yr Jendersie et al., 2018) with catchment scale mass balance studies (47.7 Gt/yr, ~ 10 cm/yr Rignot et al., 2013; B. Smith et al., 2020). These rates are small in comparison to the rates confined to the channels we measured near the grounding zone of Beardmore Glacier, where continuity assumptions and channel cross-sectional area suggest melt rates exceed 20 m/yr.

Elevation models of the network of channels we image in radar data suggest that channels correspond to local surface depressions (Figures 3 and 4). Surface elevation observations suggest that the primary channel we observe in our radar survey is one of at least nine basal channels. Most of the smaller channels initiate west of the primary basal channel we observe in radar data. These smaller channels appear to combine into the primary channel downstream as the ice shelf is sheared flowing into the Ross Sea.

Based on the inland extent of mapped surface depressions in satellite imagery and radar evidence for conduits upstream of the grounding zone, we deduce that the high melt rates that incise the channels at the Beardmore grounding zone are linked to freshwater subglacial discharge. The cross-sectional area of the primary conduit, A_c , we observe upstream of the grounding zone can be used with assumptions for the pressure gradient, G , to estimate the discharge flux, Q_d , according to R othlisberger channel theory

$$Q_d = \sqrt{\frac{G}{4\pi^{2/3}\rho_w g n_m^2 A_c^{-8/3}}} \quad (6)$$

where ρ_w is the density of water and n_m denotes the Manning roughness coefficient, a parameter with values ranging from 10^{-2} to 10^{-1} s·m^{1/3} (Cuffey & Paterson, 2010; R othlisberger, 1972). Using this relationship and assuming a pressure gradient consistent with the change in overburden pressure near the grounding zone, we find that the discharge flux of the primary channel we image with radar (blue vertical line Figure 5b R othlisberger, 1972), is larger than the entire discharge flux of the Beardmore catchment estimated from altimetry data (red vertical line; Figures 5b, Willis et al., 2016). The large, seemingly inconsistent width of the channel we observe inland of the grounding zone may be explained by groundwater infiltration where the channel initiates in radar data. Seawater intrusion inland of the grounding zone has been observed beneath Thwaites Glacier, West Antarctica (Rignot et al., 2024). Models that represent sea-water infiltration suggest that melt rates inland of the grounding zone can be enhanced by an order of magnitude above background rates (Bradley & Hewitt, 2024).

For ambient ocean temperatures expected at our study site (-2.3 to -2.0 °C), a grounding-line discharge flux of at least 7.5×10^{-2} m²/s is required for the melt rates simulated with the radially averaged plume model to be consistent with the peak melt rates we determine from continuity calculations for a single channel. These discharge fluxes are large and appear to conflict with thermomechanical model results, which indicate that Beardmore Glacier is frozen to the bed across large areas of the upstream catchment (Golledge et al., 2014).

Our plume model simulations consider the shear-driven ice shelf-ocean boundary layer regime, in which melt rate can be parameterized as the product of friction velocity and thermal driving along the channel. The pressure gradient that likely drives the flow along the base of the channel roof is larger than the pressure gradients outside the channel, where the along-flow slopes calculated from radar profiles of the ice shelf are less steep than the slope of the ambient ice-shelf draft. These slopes along the channel and outside of the channel are still small ($\sin(\alpha) = 0.01 - 0.001$, where α is the angle from the horizontal) compared to the slopes that characterize the walls of the channel ($\sin(\alpha) = 0.1 - 0.6$). These steep slopes at the sides of the channel combined with the geostrophic circulation within the cavity may promote cross channel circulation (e.g., Millgate et al., 2013; Sergienko, 2013) that would not be resolved in 1D, radially averaged models of plume circulation (Cowton et al., 2015; Jenkins, 2011).

Recent 3D simulations of idealized ice-shelf channel boundary layer currents that can resolve cross-channel shear suggest that the geometry of the channel may lead to substantial amplification of plume warming, salination and melt within ice-shelf channels (Cheng et al., 2024). As channels incise deeper into the base of ice shelves, the steepening of the channel flanks enhances diffusivity where the rapid inflow of glacial meltwater shears past ambient ocean water (Cheng et al., 2024). This mixing warms and salinizes the glacial meltwater that flows faster as the channel incises deeper into the shelf (Cheng et al., 2024). For the Beardmore channels, geostrophic inflow would introduce mixing on the eastern channel flanks and tilt isopycnals westward within the channels, enhancing melt and recirculation of modified glacial meltwater on the western channel flanks. This could explain the asymmetric geometry we observe in cross-channel profiles that is consistent with higher melt rates on the western edge of the channels observed for the Beardmore Glacier channels and channels observed elsewhere in Antarctica (Figure 2; Humbert et al., 2022; Alley et al., 2024). High melt rates (20–30 m/yr) in a cold shelf cavity confined to a narrow channel are consistent with the findings of (Cheng et al., 2024) that suggest melting within channels can be enhanced by ice-shelf channel geometry. Future work should apply 3D ocean current models like the model presented by Cheng et al. (2024) to much narrower basal topographic features with very steep sidewalls presented here and combine models with growing in situ autonomous robotic observations to explore the oceanic processes and hydrographic properties within these features. These efforts and in situ observations should mirror high-resolution satellite derived melt-rate observational studies to characterize the spatial wavenumber dependence of melt rates across Antarctic ice shelves. More observations should be used to refine this relationship (see Text S5 in Supporting Information S1) across warm and cold shelf environments and for geometries that span the range of channel shapes we see beneath Antarctic ice shelves.

5. Conclusions

We present ice-penetrating radar and satellite remote sensing observations of the geometry and englacial layering in the vicinity of a system of basal-melt channels across the Beardmore Glacier grounding zone. Our data clearly show that cold-cavity ice shelves can host large basal channels with well-developed terrace-like sidewalls. These channels initiate inland from the grounding zone, seeded by the drainage of fresh subglacial meltwater to the ocean. The concentrated basal melt within the channel minimally affects the ice-shelf englacial velocity structure near the grounding zone, resulting in very little secondary flow into the channel. The basal-melt rates (>20 m/yr) indicated by the channel incision are more than 27× higher than ambient Ross Ice Shelf Cavity melt rates (0.076 m/yr; Stevens et al., 2020), and suggest subglacial discharge and enhanced entrainment due to cross-channel circulation may be active once sufficient vertical channel walls develop.

Data Availability Statement

All radar data can be accessed from the United States Antarctic Program Data Center (Conway, 2018; Hoffman et al., 2023). Software for all of the code to simulate the idealized plume into the channel are available at Hoffman and Anselin (2025).

References

- Alley, K. E., Alley, R. B., Crawford, A. D., Ochwat, N., Wild, C. T., Marson, J., et al. (2024). Evolution of sub-ice-shelf channels reveals changes in ocean-driven melt in west Antarctica. *Journal of Glaciology*, 70, 1–15. <https://doi.org/10.1017/jog.2024.20>
- Alley, K. E., Scambos, T. A., Alley, R. B., & Holschuh, N. (2019). Troughs developed in ice-stream shear margins precondition ice shelves for ocean-driven breakup. *Science Advances*, 5(10), eaax2215. <https://doi.org/10.1126/sciadv.aax2215>
- Alley, K. E., Scambos, T. A., Anderson, R. S., Rajaram, H., Pope, A., & Haran, T. M. (2018). Continent-wide estimates of Antarctic strain rates from Landsat 8-derived velocity grids. *Journal of Glaciology*, 64(244), 321–332. <https://doi.org/10.1017/jog.2018.23>
- Alley, K. E., Scambos, T. A., Siegfried, M. R., & Fricker, H. A. (2016). Impacts of warm water on Antarctic ice shelf stability through basal channel formation. *Nature Geoscience*, 9(4), 290–293. <https://doi.org/10.1038/ngeo2675>
- Bartos, M. (2020). PYSHEDS: Simple and fast watershed delineation in python. <https://doi.org/10.5281/zenodo.3822494>
- Bradley, A. T., & Hewitt, I. J. (2024). Tipping point in ice-sheet grounding-zone melting due to ocean water intrusion. *Nature Geoscience*, 17(7), 631–637. <https://doi.org/10.1038/s41561-024-01465-7>
- Burchard, H., Bolding, K., Jenkins, A., Losch, M., Reinert, M., & Umlauf, L. (2022). The vertical structure and entrainment of subglacial melt water plumes. *Journal of Advances in Modeling Earth Systems*, 14(3), e2021MS002925. <https://doi.org/10.1029/2021MS002925>
- Cai, W., Jia, F., Li, S., Purich, A., Wang, G., Wu, L., et al. (2023). Antarctic shelf ocean warming and sea ice melt affected by projected El Niño changes. *Nature Climate Change*, 13(3), 235–239. <https://doi.org/10.1038/s41558-023-01610-x>
- Chartrand, A. M., & Howat, I. M. (2020). Basal channel evolution on the Getz ice shelf, west Antarctica. *Journal of Geophysical Research: Earth Surface*, 125(9), e2019JF005293. <https://doi.org/10.1029/2019JF005293>
- Cheng, C., Jenkins, A., Holland, P. R., Wang, Z., Dong, J., & Liu, C. (2024). Ice shelf basal channel shape determines channelized ice-ocean interactions. *Nature Communications*, 15(1), 2877. <https://doi.org/10.1038/s41467-024-47351-z>

Acknowledgments

We recognize the work of Maurice Conway, Richard Hindmarsh, Max Stevens and Michael Hay who helped collect the data presented in this study. This study was funded by the US National Science Foundation (Awards 1141889 and 1141866), and the National Aeronautics and Space Administration (FINESST Award 80NSSC20K1627 and 80NSSC22K0381). Digital elevation models were provided by the Polar Geospatial Center. We also acknowledge the tremendous intellectual support of the late Dr. Richard Hindmarsh without whom this work would not have been possible.

- Christianson, K., Bushuk, M., Dutrieux, P., Parizek, B. R., Joughin, I. R., Alley, R. B., et al. (2016). Sensitivity of Pine Island Glacier to observed ocean forcing. *Geophysical Research Letters*, *43*(20), 10817–10825. <https://doi.org/10.1002/2016gl070500>
- Christianson, K., Jacobel, R. W., Horgan, H. J., Alley, R. B., Anandakrishnan, S., Holland, D. M., & DallaSanta, K. J. (2016). Basal conditions at the grounding zone of Whillans Ice Stream, West Antarctica, from ice-penetrating radar. *Journal of Geophysical Research: Earth Surface*, *121*(11), 1954–1983. <https://doi.org/10.1002/2015jf003806>
- Conway, H. (2018). Geophysical measurements Beardmore Glacier, Antarctica. <https://doi.org/10.15784/601121>
- Conway, H., Smith, B., Vaswani, P., Matsuoka, K., Rignot, E., & Claus, P. (2009). A low-frequency ice-penetrating radar system adapted for use from an airplane: Test results from bering and malaspina glaciers, Alaska, USA. *Annals of Glaciology*, *50*(51), 93–97. <https://doi.org/10.3189/172756409789097487>
- Cowton, T., Slater, D., Sole, A., Goldberg, D., & Nienow, P. (2015). Modeling the impact of glacial runoff on fjord circulation and submarine melt rate using a new subgrid-scale parameterization for glacial plumes. *Journal of Geophysical Research: Oceans*, *120*(2), 796–812. <https://doi.org/10.1002/2014JC010324>
- Cuffey, K. M., & Paterson, W. S. B. (2010). *The physics of glaciers*. Academic Press.
- Drews, R., Pattyn, F., Hewitt, I. J., Ng, F. S. L., Berger, S., Matsuoka, K., et al. (2017). Actively evolving subglacial conduits and eskers initiate ice shelf channels at an Antarctic grounding line. *Nature Communications*, *8*(1), 15228. <https://doi.org/10.1038/ncomms15228>
- Drews, R., Schannwell, C., Ehlers, T. A., Gladstone, R., Pattyn, F., & Matsuoka, K. (2020). Atmospheric and oceanographic signatures in the ice shelf channel morphology of Roi Baudouin Ice Shelf, East Antarctica, inferred from radar data. *Journal of Geophysical Research: Earth Surface*, *125*(7), e2020JF005587. <https://doi.org/10.1029/2020jf005587>
- Dutrieux, P., Stewart, C., Jenkins, A., Nicholls, K. W., Corr, H. F., Rignot, E., & Steffen, K. (2014). Basal terraces on melting ice shelves. *Geophysical Research Letters*, *41*(15), 5506–5513. <https://doi.org/10.1002/2014GL060618>
- Gades, A. M., Raymond, C. F., Conway, H., & Jacobel, R. W. (2000). Bed properties of Siple Dome and adjacent ice streams, West Antarctica, inferred from radio-echo sounding measurements. *Journal of Glaciology*, *46*(152), 88–94. <https://doi.org/10.3189/172756500781833467>
- Gladish, C. V., Holland, D. M., Holland, P. R., & Price, S. F. (2012). Ice-shelf basal channels in a coupled ice/ocean model. *Journal of Glaciology*, *58*(212), 1227–1244. <https://doi.org/10.3189/2012JG12J003>
- Golledge, N. R., Marsh, O. J., Rack, W., Braaten, D., & Jones, R. S. (2014). Basal conditions of two Transantarctic Mountains outlet glaciers from observation-constrained diagnostic modelling. *Journal of Glaciology*, *60*(223), 855–866. <https://doi.org/10.3189/2014jog13j131>
- Hills, B. H., Christianson, K., Holschuh, N. (2020). A framework for attenuation method selection evaluated with ice-penetrating radar data at South Pole Lake. *Annals of Glaciology*, *61*(81), 176–187. <https://doi.org/10.1017/aog.2020.32>
- Hoffman, A. O., & Anselin, J. (2025). Point source submarine melt water plume model [Software]. *Zenodo*. <https://doi.org/10.5281/zenodo.15259312>
- Hoffman, A. O., Christianson, K., & Conway, H. (2023). Beardmore Glacier high-frequency impulse radar data. *USAP DC*. <https://doi.org/10.15784/601713>
- Holland, D. M., & Jenkins, A. (1999). Modeling thermodynamic ice-ocean interactions at the base of an ice shelf. *Journal of Physical Oceanography*, *29*(8), 1787–1800. [https://doi.org/10.1175/1520-0485\(1999\)029<1787:mtioia>2.0.co;2](https://doi.org/10.1175/1520-0485(1999)029<1787:mtioia>2.0.co;2)
- Howat, I. M., Porter, C., Smith, B. E., Noh, M.-J., & Morin, P. (2019). The reference elevation model of Antarctica. *The Cryosphere*, *13*(2), 665–674. <https://doi.org/10.5194/tc-13-665-2019>
- Humbert, A., Christmann, J., Corr, H. F. J., Helm, V., Höyns, L.-S., Hofstede, C., et al. (2022). On the evolution of an ice shelf melt channel at the base of Filchner Ice Shelf, from observations and viscoelastic modeling. *The Cryosphere*, *16*(10), 4107–4139. <https://doi.org/10.5194/tc-16-4107-2022>
- Jendersie, S., Williams, M. J., Langhorne, P. J., & Robertson, R. (2018). The density-driven winter intensification of the ross sea circulation. *Journal of Geophysical Research: Oceans*, *123*(11), 7702–7724. <https://doi.org/10.1029/2018jc013965>
- Jenkins, A. (1991). A one dimensional model of ice-ocean interaction. *Journal of Geophysical Research*, *96*(C11), 671–677.
- Jenkins, A. (2011). Convection-driven melting near the grounding lines of ice shelves and tidewater glaciers. *Journal of Physical Oceanography*, *41*(12), 2279–2294. <https://doi.org/10.1175/JPO-D-11-03.1>
- Le Brocq, A. M., Payne, A. J., & Vieli, A. (2010). An improved Antarctic dataset for high resolution numerical ice sheet models (ALBMAP v1). *Earth System Science Data*, *2*(2), 247–260. <https://doi.org/10.5194/essd-2-247-2010>
- Le Brocq, A. M., Ross, N., Griggs, J. A., Bingham, R. G., Corr, H. F. J., Ferraccioli, F., et al. (2013). Evidence from ice shelves for channelized meltwater flow beneath the Antarctic Ice Sheet. *Nature Geoscience*, *6*(11), 945–948. <https://doi.org/10.1038/ngeo1977>
- Lilien, D. A., Hills, B. H., Driscoll, J., Jacobel, R., & Christianson, K. (2020). ImpDAR: An open-source impulse radar processor. *Annals of Glaciology*, *61*(81), 114–123. <https://doi.org/10.1017/aog.2020.44>
- MacAyeal, D. R. (1984). Thermohaline circulation below the Ross Ice Shelf: A consequence of tidally induced vertical mixing and basal melting. *Journal of Geophysical Research*, *89*(C1), 597–606. <https://doi.org/10.1029/jc089ic01p00597>
- MacGregor, J. A., Li, J., Paden, J. D., Catania, G. A., Clow, G. D., Fahnestock, M. A., et al. (2015). Radar attenuation and temperature within the Greenland Ice Sheet. *Journal of Geophysical Research: Earth Surface*, *120*(6), 983–1008. <https://doi.org/10.1002/2014jft003418>
- Marsh, O. J., Fricker, H. A., Siegfried, M. R., Christianson, K., Nicholls, K. W., Corr, H. F. J., & Catania, G. (2016). High basal melting forming a channel at the grounding line of Ross Ice Shelf, Antarctica. *Geophysical Research Letters*, *43*(1), 250–255. <https://doi.org/10.1002/2015gl066612>
- Matsuoka, K., Morse, D., & Raymond, C. F. (2010). Estimating englacial radar attenuation using depth profiles of the returned power, central West Antarctica. *Journal of Geophysical Research*, *115*(F2), F02012. <https://doi.org/10.1029/2009jf001496>
- McPhee, M. G., Maykut, G. A., & Morison, J. H. (1987). Dynamics and thermodynamics of the ice/upper ocean system in the marginal ice zone of the Greenland Sea. *Journal of Geophysical Research*, *92*(C7), 7017–7031. <https://doi.org/10.1029/JC092iC07p07017>
- Mernild, S. H., Howat, I. M., Ahn, Y., Liston, G. E., Steffen, K., Jakobsen, B. H., et al. (2010). Freshwater flux to sermilik fjord, SE Greenland. *The Cryosphere*, *4*(4), 453–465. <https://doi.org/10.5194/tc-4-453-2010>
- Millgate, T., Holland, P. R., Jenkins, A., & Johnson, H. L. (2013). The effect of basal channels on oceanic ice-shelf melting. *Journal of Geophysical Research: Oceans*, *118*(12), 6951–6964. <https://doi.org/10.1002/2013JC009402>
- Morlighem, M., Rignot, E., Binder, T., Blankenship, D., Drews, R., Eagles, G., et al. (2020). Deep glacial troughs and stabilizing ridges unveiled beneath the margins of the Antarctic ice sheet. *Nature Geoscience*, *13*(2), 132–137. <https://doi.org/10.1038/s41561-019-0510-8>
- Morton, B. R., Taylor, G., & Turner, J. S. (1956). Turbulent gravitational convection from maintained and instantaneous sources. *Proceedings of the Royal Society of London*, *234A*, 1–23.
- Mouginot, J., Rignot, E., & Scheuchl, B. (2019). Continent-wide, interferometric SAR phase, mapping of Antarctic ice velocity. *Geophysical Research Letters*, *46*(16), 9710–9718. <https://doi.org/10.1029/2019GL083826>

- Naughten, K. A., Holland, P. R., & De Rydt, J. (2023). Unavoidable future increase in west Antarctic ice-shelf melting over the twenty-first century. *Nature Climate Change*, *13*(11), 1222–1228. <https://doi.org/10.1038/s41558-023-01818-x>
- Nicholls, K. W., Østerhus, S., Makinson, K., Gammelsrød, T., & Fahrback, E. (2009). Ice-ocean processes over the continental shelf of the southern Weddell Sea. *Antarctica: A review*, *47*(3), RG3003. <https://doi.org/10.1029/2007RG000250>
- Nuth, C., & Kääb, A. (2011). Co-registration and bias corrections of satellite elevation data sets for quantifying glacier thickness change. *The Cryosphere*, *5*(1), 271–290. <https://doi.org/10.5194/tc-5-271-2011>
- Paolo, F. S., Fricker, H. A., & Padman, L. (2015). Volume loss from Antarctic ice shelves is accelerating. *Science*, *348*(6232), 327–331. <https://doi.org/10.1126/science.aaa0940>
- Reese, R., Gudmundsson, G. H., Levermann, A., Winkelmann, R. (2018). The far reach of ice-shelf thinning in Antarctica. *Nature Climate Change*, *8*(1), 53–57. <https://doi.org/10.1038/s41558-017-0020-x>
- Rignot, E., Ciraci, E., Scheuchl, B., Tolpekin, V., Wollersheim, M., & Dow, C. (2024). Widespread seawater intrusions beneath the grounded ice of Thwaites glacier, west Antarctica. *Proceedings of the National Academy of Sciences*, *121*(22), e2404766121. <https://doi.org/10.1073/pnas.2404766121>
- Rignot, E., Jacobs, S., Mougnot, J., & Scheuchl, B. (2013). Ice-shelf melting around Antarctica. *Science*, *341*(6143), 266–270. <https://doi.org/10.1126/science.1235798>
- Rignot, E., Mougnot, J., Scheuchl, B., Broeke, M. v. d., Wessem, M. J. v., & Morlighem, M. (2019). Four decades of Antarctic Ice Sheet mass balance from 1979–2017. *Proceedings of the National Academy of Sciences*, *116*(4), 1095–1103. <https://doi.org/10.1073/pnas.1812883116>
- Rignot, E., & Steffen, K. (2008). Channelized bottom melting and stability of floating ice shelves. *Geophysical Research Letters*, *35*(2), L02503. <https://doi.org/10.1029/2007GL031765>
- Rosevear, M. G., Gayen, B., & Galton-Fenzi, B. K. (2022). Regimes and transitions in the basal melting of Antarctic ice shelves. *Journal of Physical Oceanography*, *52*(10), 2589–2608. <https://doi.org/10.1175/JPO-D-21-0317.1>
- Röthlisberger, H. (1972). Water pressure in intra- and subglacial channels. *Journal of Glaciology*, *11*(62), 177–203. <https://doi.org/10.3189/S0022143000022188>
- Sergienko, O. V. (2013). Basal channels on ice shelves. *Journal of Geophysical Research: Earth Surface*, *118*(3), 1342–1355. <https://doi.org/10.1002/jgrf.20105>
- Shean, D., Swinski, J., Smith, B., Sutterley, T., Henderson, S., Ugarte, C., et al. (2023). Sliderule: Enabling rapid, scalable, open science for the NASA ICESat-2 mission and beyond. *Journal of Open Source Software*, *8*(81), 4982. <https://doi.org/10.21105/joss.04982>
- Shean, D. E., Joughin, I. R., Dutrieux, P., Smith, B. E., & Berthier, E. (2019). Ice shelf basal melt rates from a high-resolution digital elevation model (DEM) record for Pine Island Glacier, Antarctica. *The Cryosphere*, *13*(10), 2633–2656. <https://doi.org/10.5194/tc-13-2633-2019>
- Smith, B., Fricker, H. A., Gardner, A. S., Medley, B., Nilsson, J., Paolo, F. S., et al. (2020). Pervasive ice sheet mass loss reflects competing ocean and atmosphere processes. *Science*, *368*(6496), 1239–1242. <https://doi.org/10.1126/science.aaz5845>
- Smith, B. E., Fricker, H. A., Joughin, I. R., & Tulaczyk, S. (2009). An inventory of active subglacial lakes in Antarctica detected by ICESat (2003–2008). *Journal of Glaciology*, *55*(192), 573–595. <https://doi.org/10.3189/002214309789470879>
- Stanton, T. P., Shaw, W. J., Truffer, M., Corr, H. F. J., Peters, L. E., Riverman, K. L., et al. (2013). Channelized ice melting in the ocean boundary layer beneath pine island glacier, Antarctica. *Science*, *341*(6151), 1236–1239. <https://doi.org/10.1126/science.1239373>
- Stevens, C., Hulbe, C., Brewer, M., Stewart, C., Robinson, N., Ohneiser, C., & Jendersie, S. (2020). Ocean mixing and heat transport processes observed under the Ross Ice Shelf control its basal melting. *Proceedings of the National Academy of Sciences of the United States of America*, *117*(29), 16799–16804. <https://doi.org/10.1073/pnas.1910760117>
- Stewart, C. L. (2018). *Ice-ocean interactions beneath the north-western Ross ice shelf, Antarctica (unpublished doctoral dissertation)*. Old Dominion University.
- Vreugdenhil, C. A., & Taylor, J. R. (2019). Stratification effects in the turbulent boundary layer beneath a melting ice shelf: Insights from resolved large-eddy simulations. *Journal of Physical Oceanography*, *49*(7), 1905–1925. <https://doi.org/10.1175/JPO-D-18-0252.1>
- Watkins, R. H., Bassis, J. N., & Thouless, M. D. (2021). Roughness of ice shelves is correlated with basal melt rates. *Geophysical Research Letters*, *48*(21), e2021GL094743. <https://doi.org/10.1029/2021GL094743>
- Whiteford, A., Horgan, H. J., Leong, W. J., & Forbes, M. (2022). Melting and refreezing in an ice shelf basal channel at the grounding line of the Kamb ice stream, west Antarctica. *Journal of Geophysical Research: Earth Surface*, *127*(11), e2021JF006532. <https://doi.org/10.1029/2021JF006532>
- Willis, I. C., Pope, E. L., Vieli, G. J.-M. L., Arnold, N. S., & Long, S. (2016). Drainage networks, lakes and water fluxes beneath the Antarctic ice sheet. *Annals of Glaciology*, *57*(72), 96–108. <https://doi.org/10.1017/aog.2016.15>

References From the Supporting Information

- Bindschadler, R., Choi, H., Wichlacz, A., Bingham, R., Bohlander, J., Brunt, K., et al. (2011). Getting around Antarctica: New high-resolution mappings of the grounded and freely-floating boundaries of the Antarctic ice sheet created for the International Polar Year. *The Cryosphere*, *5*(3), 569–588. <https://doi.org/10.5194/tc-5-569-2011>
- Bindschadler, R., Vaughan, D. G., & Vormberger, P. (2011). Variability of basal melt beneath the Pine Island Glacier ice shelf, West Antarctica. *Journal of Glaciology*, *57*(204), 581–595. <https://doi.org/10.3189/002214311797409802>
- Bogorodsky, V. V., Bentley, C. R., & Gudmandsen, P. E. (1985). *Radioglaciology*. Springer Dordrecht.
- Corr, H. F. J., Jenkins, A., Nicholls, K. W., & Doake, C. S. M. (2002). Precise measurement of changes in ice-shelf thickness by phase-sensitive radar to determine basal melt rates. *Geophysical Research Letters*, *29*(8). <https://doi.org/10.1029/2001gl014618>
- Fujita, S., Maeno, H., & Matsuoka, K. (2006). Radio-wave depolarization and scattering within ice sheets: A matrix-based model to link radar and ice-core measurements and its application. *Journal of Glaciology*, *52*(178), 407–424. <https://doi.org/10.3189/172756506781828548>
- Gillet-Chaulet, F., Hindmarsh, R. C. A., Corr, H. F. J., King, E. C., & Jenkins, A. (2011). In-situ quantification of ice rheology and direct measurement of the Raymond Effect at Summit, Greenland using a phase-sensitive radar. *Geophysical Research Letters*, *38*(24), L24503. <https://doi.org/10.1029/2011gl049843>
- Holland, P. R., Jenkins, A., & Holland, D. M. (2008). The response of Ice shelf basal melting to variations in ocean temperature. *Journal of Climate*, *21*(11), 2558–2572. <https://doi.org/10.1175/2007JCLI1909.1>
- Jacobel, R. W., Welch, B. C., Osterhouse, D., Pettersson, R., & MacGregor, J. A. (2009). Spatial variation of radar-derived basal conditions on Kamb Ice Stream, West Antarctica. *Annals of Glaciology*, *50*(51), 10–16. <https://doi.org/10.3189/172756409789097504>
- Jenkins, A., Corr, H. F., Nicholls, K. W., Stewart, C. L., & Doake, C. S. (2006). Interactions between ice and ocean observed with phase-sensitive radar near an Antarctic ice-shelf grounding line. *Journal of Glaciology*, *52*(178), 325–346. <https://doi.org/10.3189/172756506781828502>

- Marsh, O. J., Rack, W., Floricioiu, D., Gолledge, N. R., & Lawson, W. (2013). Tidally induced velocity variations of the Beardmore Glacier, Antarctica, and their representation in satellite measurements of ice velocity. *The Cryosphere*, 7(5), 1375–1384. <https://doi.org/10.5194/tc-7-1375-2013>
- Matsuoka, K., MacGregor, J. A., & Pattyn, F. (2012). Predicting radar attenuation within the Antarctic ice sheet. *Earth and Planetary Science Letters*, 359, 173–183. <https://doi.org/10.1016/j.epsl.2012.10.018>
- Matsuoka, K., Wilen, L., Hurley, S. P., & Raymond, C. F. (2009). Effects of birefringence within ice sheets on obliquely propagating radio waves. *IEEE Transactions on Geoscience and Remote Sensing*, 47(5), 1429–1443. <https://doi.org/10.1109/tgrs.2008.2005201>
- Nicholls, K. W., Corr, H. F., Stewart, C. L., Lok, L. B., Brennan, P. V., & Vaughan, D. G. (2015). A ground-based radar for measuring vertical strain rates and timevarying basal melt rates in ice sheets and shelves. *Journal of Glaciology*, 61(230), 1079–1087. <https://doi.org/10.3189/2015jog15j073>
- Winebrenner, D. P., Smith, B. E., Catania, G. A., Conway, H. B., & Raymond, C. F. (2003). Radio-frequency attenuation beneath Siple Dome, West Antarctica, from wide-angle and profiling radar observations. *Annals of Glaciology*, 37, 226–232. <https://doi.org/10.3189/172756403781815483>